

SCIENTIFIC REPORTS

OPEN

Observation of re-entrant spin reorientation in $\text{TbFe}_{1-x}\text{Mn}_x\text{O}_3$

Yifei Fang^{1,2}, Ya Yang², Xinzhi Liu³, Jian Kang², Lijie Hao³, Xiping Chen⁴, Lei Xie⁴, Guangai Sun⁴, Venkatesh Chandragiri², Chin-Wei Wang⁵, Yiming Cao², Fei Chen¹, Yuntao Liu³, Dongfeng Chen³, Shixun Cao^{1,2}, Chengtian Lin⁶, Wei Ren² & Jincang Zhang^{1,2}

Received: 12 July 2016

Accepted: 25 August 2016

Published: 16 September 2016

We report a spin reorientation from $\Gamma_4(G_x, A_y, F_z)$ to $\Gamma_1(A_x, G_y, C_z)$ magnetic configuration near room temperature and a re-entrant transition from $\Gamma_1(A_x, G_y, C_z)$ to $\Gamma_4(G_x, A_y, F_z)$ at low temperature in $\text{TbFe}_{1-x}\text{Mn}_x\text{O}_3$ single crystals by performing both magnetization and neutron diffraction measurements. The $\Gamma_4 - \Gamma_1$ spin reorientation temperature can be enhanced to room temperature when x is around 0.5–0.6. These new transitions are distinct from the well-known $\Gamma_4 - \Gamma_2$ transition observed in TbFeO_3 , and the sinusoidal antiferromagnetism to complex spiral magnetism transition observed in multiferroic TbMnO_3 . We further study the evolution of magnetic entropy change ($-\Delta S_M$) versus Mn concentration to reveal the mechanism of the re-entrant spin reorientation behavior and the complex magnetic phase at low temperature. The variation of $-\Delta S_M$ between a and c axes indicates the significant change of magnetocrystalline anisotropy energy in the $\text{TbFe}_{1-x}\text{Mn}_x\text{O}_3$ system. Furthermore, as Jahn-Teller inactive Fe^{3+} ions coexist with Jahn-Teller active Mn^{3+} ions, various anisotropy interactions, compete with each other, giving rise to a rich magnetic phase diagram. The large magnetocaloric effect reveals that the studied material could be a potential magnetic refrigerant. These findings expand our knowledge of spin reorientation phenomena and offer the alternative realization of spin-switching devices at room temperature in the rare-earth orthoferrites.

The rare-earth orthoferrites RFeO_3 (R = rare-earth elements) is a family of functional materials with large magnetoelectric (ME) coupling and optomagnetic properties^{1,2}. Some of RFeO_3 have been reported to be multiferroic materials with possible applications^{3–5}. Furthermore, spin reorientation phase transition in such antiferromagnetic (AFM) insulators has attracted much attention since high-temperature $\Gamma_4(G_x, A_y, F_z)$ phase usually transforms to $\Gamma_2(F_x, C_y, G_z)$ at lower temperature³. Meanwhile, the rare-earth manganites RMnO_3 , aroused great interest in spintronics due to both colossal magnetoresistance (CMR) and magnetoelectric coupling effects^{6–11}. The neutron diffraction experiments have revealed the existence of helical spin structure in RMnO_3 (R = Tb, Dy) systems^{12–15} being the origin of their magnetoelectric coupling effect^{16–19}.

The compounds of TbMnO_3 and TbFeO_3 both belong to the orthorhombic space group $Pbnm$ with the same distorted perovskite structure. But they show distinct magnetic properties due to their totally different spin configurations. TbFeO_3 has a canted AFM spin ordering caused by the Dzyaloshinskii-Moriya (DM) interaction⁵. Previous reports confirmed that most RFeO_3 (R = Tb, Er, Sm, Tm, Yr, Sc, Nd, etc.) should undergo a spin reorientation transition from Γ_4 to Γ_2 ^{3,5,20–28}, as a second-order magnetic phase transition. Exceptionally, DyFeO_3 exhibits an interesting $\Gamma_4 \rightarrow \Gamma_1(A_x, G_y, C_z)$ phase transition which completely annihilates weak magnetic moments observed in $\Gamma_4(F_z)$ or $\Gamma_2(F_x)$, along any crystallographic direction. This phenomenon has been observed in magnetization measurement, but not yet detected by neutron diffraction experiment due to the high absorption of Dy element. On the other hand, TbMnO_3 manifests both magnetoelectric and magnetocaloric effect^{29,30}, the latter is a key ingredient for high efficient magnetic refrigerant with large magnetic entropy change ($-\Delta S_M$). It was previously shown that the spiral spin structures of Mn^{3+} ions below 27 K lead to ferroelectricity²⁹ and mutual controls of magnetism and electricity^{14,31}. However, the spiral spin order is weak and can be easily destroyed by doping transition metals. Thus, although the parent compounds without doping are well investigated, the rich physics due to off-stoichiometry $\text{TbFe}_{1-x}\text{Mn}_x\text{O}_3$ is largely unexplored. It is our goal of present work to find out

¹Materials Genome Institute, Shanghai University, Shanghai 200444, China. ²Department of Physic, Shanghai University, Shanghai 200444, China. ³Neutron Scattering Laboratory, China Institute of Atomic Energy, Beijing 102413, China. ⁴Institute of Nuclear Physics and Chemistry, China Academy of Engineering Physics, Mianyang 621999, China. ⁵ANSTO, Kirrawee Dc, NSW 2232, Australia. ⁶Max Planck Institute for Solid State Research, Heisenbergstraße 1, D-70569 Stuttgart, Germany. Correspondence and requests for materials should be addressed to W.R. (email: renwei@shu.edu.cn) or J.Z. (email: jczhang@shu.edu.cn)

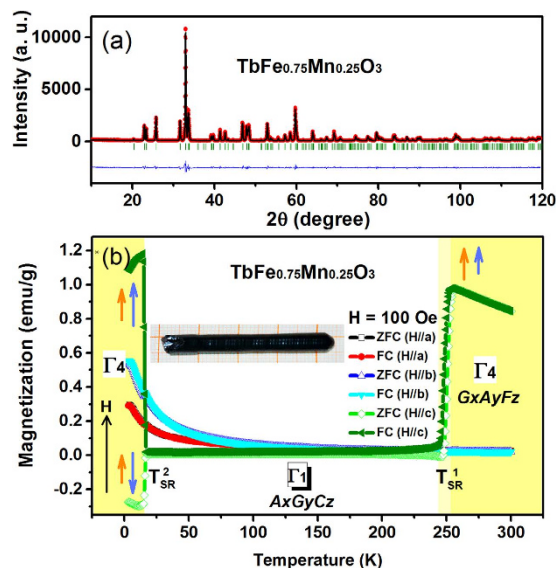


Figure 1. Powder XRD refinement and magnetic phase transition of $\text{TbMn}_{0.25}\text{Fe}_{0.75}\text{O}_3$. (a) XRD patterns obtained by the ground crystal powders at room temperature. Inset is the optical-floating-zone grown single crystal on a grid of millimeter. (b) The temperature dependence of magnetization curves under $H = 100$ Oe. The shaded parts denote the magnetic phase transition and divarication of ZFC/FC. The arrows show the evolution of magnetization arising from Tb (blue) and Fe/Mn (orange).

new magnetic phase and reveal the mechanism of new spin reorientation in $\text{TbFe}_{1-x}\text{Mn}_x\text{O}_3$ system, from which some remarkable behaviors expected to be found due to competitive magnetic phases that do not exist in both TbMnO_3 and TbFeO_3 .

In this work, we synthesized a series of $\text{TbFe}_{1-x}\text{Mn}_x\text{O}_3$ and reported their special magnetic phase transitions by performing magnetization and neutron powder diffraction (NPD) measurements. We demonstrate that the phase transition of $\Gamma_4 \rightarrow \Gamma_1 \rightarrow \Gamma_4$ exists in $\text{TbFe}_{0.75}\text{Mn}_{0.25}\text{O}_3$ single crystal, rather than the common transition of $\Gamma_4 \rightarrow \Gamma_2$ as observed in TbFeO_3 and other orthoferrites. From a practical point of view, $\Gamma_4 \rightarrow \Gamma_1$ (weak magnetic moment to zero net moment) transition may find use even with easily-obtained polycrystalline samples whereas we need to grow single crystals to observe $\Gamma_4 \rightarrow \Gamma_2$ (weak magnetic moment along c to a direction) transition. The magnitude of the magnetocaloric effect is found to be large and strictly resembles the observed magnetic features. The evolution of entropy change versus Mn doping are presented and discussed with in the scenario of Mn substitution-induced anisotropic interaction.

Results

Magnetometry and neutron diffraction measurements. The x-ray diffraction patterns for the $\text{TbFe}_{1-x}\text{Mn}_x\text{O}_3$ with $x = 0.25$ are plotted in Fig. 1(a). The Rietveld refinement results show that the sample has a distorted orthorhombic perovskite structure ($Pbnm$) and no additional phases are identified. Figure 1(b) shows its temperature dependence of ZFC and FC magnetization curves with $H = 100$ Oe along the a ($H||a$), b ($H||b$) and c ($H||c$) directions, denoted as $M_{ZFC}^a(M_{FC}^a)$, $M_{ZFC}^b(M_{FC}^b)$, and $M_{ZFC}^c(M_{FC}^c)$. The total magnetic moment is parallel to c axis between 254 and 300 K. A sharp drop in $M_{ZFC}^c(M_{FC}^c)$ occurs between 254 and 245 K, signaling the spin reorientation transition of Fe^{3+} ions²³. When the temperature is between 16 and 254 K, the sample shows an antiferromagnetic state for $H||c$, while both $M_{ZFC}^a(M_{FC}^a)$ and $M_{ZFC}^b(M_{FC}^b)$ increase slowly for $H||a$ and $H||b$ with the decreasing temperature. This resembles the phase transition of $\Gamma_4 \rightarrow \Gamma_1$ spin reorientation at $T_{SR} = 254$ K. Thus, we speculate that the magnetic structure transforms from the canted antiferromagnetism with weak ferromagnetism along the c axis (G_x, A_y, F_z) to the major G-type antiferromagnetic vector along the b axis (A_x, G_y, C_z). In this case, there is no net magnetic moment along the c axis in the wide range of temperature between 16 and 254 K. Interestingly, as temperature decreases below 16 K, the magnetic moment along the c axis turns to be negative with a possible (G_x, A_y, F_z) configuration in negative magnetization state. The moment configuration speculated from the magnetometry is shown as the arrows in Fig. 1(b). The arrows show the evolution of magnetization arising from Tb (blue arrows) and Fe/Mn (orange arrows), respectively. The net moments of Tb and Fe tend to keep aligning along c -axis and parallel to the direction of applied field, which is responsible for the weak ferromagnetism above T_{SR}^1 . Nevertheless, due to the $d-f$ interactions of Fe/Mn and Tb ions, the larger net moment of Tb ions become antiparallel to those of Fe ions and the direction for applied field below T_{SR}^2 in ZFC mode, leading to a negative magnetization state. However, in FC mode, both the net moments of Tb and Fe ions keep parallel to the direction of applied field, resulting in large net magnetization below T_{SR}^2 .

To confirm our speculation on the nature of the intriguing spin reorientation transition phenomena, the NPD experiments were performed and the results are shown in Fig. 2(a–c) for $T = 8, 40,$ and 300 K, respectively. All the structural Bragg peaks show no position shift or split, indicating the absence of structural phase transition at the different temperatures. Symmetry analysis was performed based on the crystal structure of $\text{TbFe}_{1-x}\text{Mn}_x\text{O}_3$

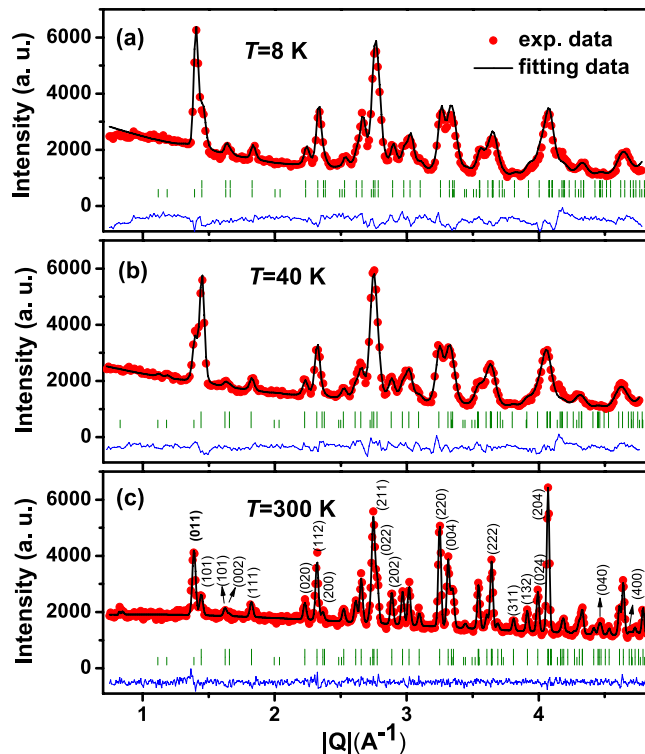


Figure 2. NPD patterns for $\text{TbFe}_{1-x}\text{Mn}_x\text{O}_3$ with $x=0.25$ sample, obtained at (a) $T=8$ K, (b) $T=40$ K and (c) $T=300$ K, respectively. The two lines of vertical bars present Bragg peaks for the crystal structures and the crystal with magnetic structures of $\text{Fe}^{3+}/\text{Mn}^{3+}$ respectively.

($x=0.25$), which is an orthorhombically-distorted perovskite structure with space group $Pbnm$. The lattice parameters for this crystal structure are $a=5.284$ Å, $b=5.603$ Å and $c=7.530$ Å. For our orthoferrites, the $k=0$ propagation vector was adopted as usual. According to the symmetry theory proposed by White³² and Bertaut²⁰, Γ_5 and Γ_8 are incompatible with a net moment on the iron sites. Γ_3 is not consistent with the observed strong antiferromagnetic coupling between nearest iron neighbors. So Γ_1 , Γ_2 and Γ_4 could be possible magnetic structure for this compound.

Then Rietveld refinements were performed to test these possibilities with the orthorhombic $Pbnm$ structure. The results show that the data obtained at 8 and 300 K fit well with the magnetic structures of $\Gamma_4(G_x, A_y, F_z)$, and the data obtained at 40 K fit well with $\Gamma_1(A_x, G_y, C_z)$. The derived structures of Fe/Mn are schematically drawn in Fig. 3(a–c), respectively. Arrows A–D represent four types of location of Fe(Mn) ions, and the corresponding refined magnetic moments along different crystallographic axes are given in supplemental material³³. Figure 3(a) illustrates an orthorhombic perovskite with Fe/Mn having G-type AFM spin order along the a axis, A-type AFM spin order along the b axis, and F-type FM spin order along the c axis, consistent to the (G_x, A_y, F_z) configuration at room temperature in Bertaut's notation²⁰. This type of commensurate spin order is observed to decline at $T_{SR}^1=254$ K and totally collapse at $T_{SR}^{1'}=245$ K, resulting in a new antiferromagnetic phase with no net magnetization along any direction³². This intriguing magnetic phase configuration is found to be A_x, G_y, C_z as shown in Fig. 3(b), instead of the common F_x, C_y, G_z reported for most RFeO_3 systems. This transition at T_{SR}^1 is characterized by the relative change of the (011) intensity and the (101) magnetic Bragg peaks around $|Q|=1.4\text{Å}^{-1}$ as shown in Fig. 2(b,c), implying that the moments of Fe^{3+} rotate from the a to b axis upon cooling as indicated in Fig. 3(a–c). With the further decrease of temperature, both $M_{ZFC}^a(M_{FC}^a)$ and $M_{ZFC}^b(M_{FC}^b)$ increase gradually. It is noted that $M_{ZFC}^c(M_{FC}^c)$ remains vanished till $T_{SR}^2=16$ K, then a sudden increase arises at T_{SR}^2 . This sharp transition from Γ_1 back to Γ_4 is accomplished within 1 K and the results are confirmed by NPD. The ordering of Tb^{3+} has not been observed at $T \geq 8$ K in our present measurement and further research at lower temperature is required. The T_{SR}^1 at 254 K is believed to be driven by both Fe–Fe and Tb–Fe/Mn sub-lattice interactions, while T_{SR}^1 at 16 K arises from the enhanced interactions of Tb–Fe/Mn sub-lattice⁵.

Spin reorientation at T_{SR}^1 . Since Γ_4 configuration is characterized by the net moments along the c axis, the magnetic phase transition of $\Gamma_4 \rightarrow \Gamma_1$ may undergo a transformation of the Fe^{3+} sublattice from weak ferromagnetism to complete antiferromagnetism upon the decreasing temperature. In order to reveal the relationship between Mn substitution and the changes in the anisotropy fields on the sublattices, a formula is developed by Holmes *et al.*²³. Based on molecular field theory, the doping concentration dependence of T_{SR}^1 obeys the following equation for $x \geq x_c$.

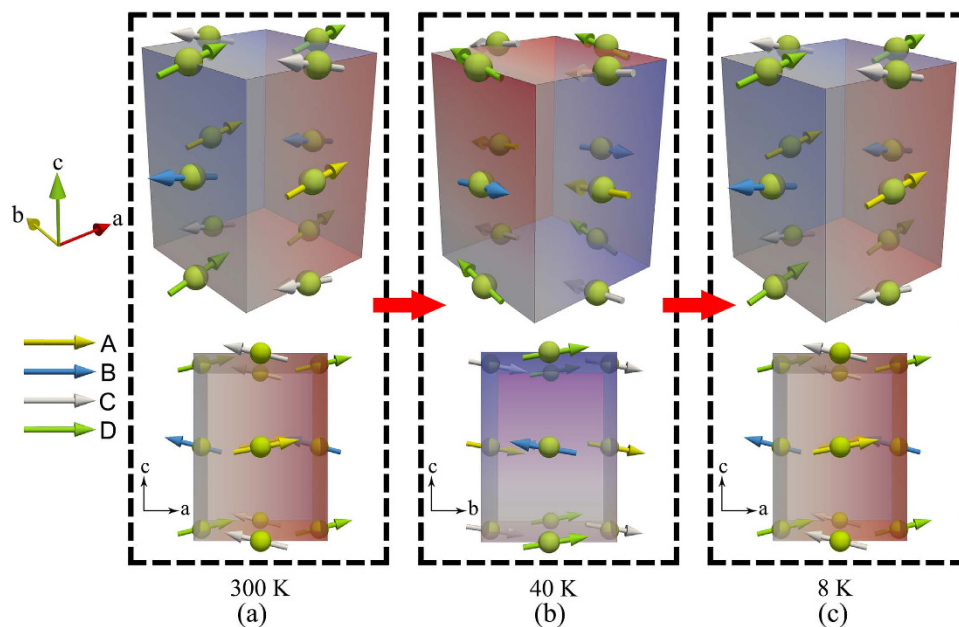


Figure 3. Evolution of magnetic phases for $\text{TbFe}_{0.75}\text{Mn}_{0.25}\text{O}_3$. The upper panels display (a) $\Gamma_4(G_x, A_y, F_z)$ phase at $T=300$ K, (b) $\Gamma_1(A_x, G_y, C_z)$ phase at $T=40$ K, and (c) $\Gamma_4(G_x, A_y, F_z)$ phase at $T=8$ K. The lower panels illustrates the side view of the upper panels, respectively. Arrows of A-D represent four kinds of spin moments of Fe(Mn) ions.

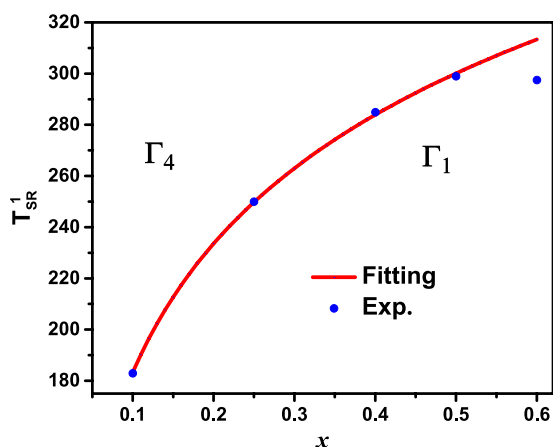


Figure 4. T_{SR}^1 as a function of x in $\text{TbFe}_{1-x}\text{Mn}_x\text{O}_3$ system. The solid line is the fitting of Eq. (1).

$$T(x) = \left(\frac{1}{k'} \right) \log \left(\frac{x}{x_c} \right) \quad (1)$$

where k' is a positive constant related to the second-order anisotropy fields in the b - a , b - c , c - a planes. x_c characterizes a critical doping concentration from a hypothesis that at $x=x_c$, the $\Gamma_4 \rightarrow \Gamma_1$ spin reorientation first appears at $T=0$ K. This formula reveals that Mn substitutions can be used to shift the $\Gamma_4 \rightarrow \Gamma_1$ spin reorientation to be near or above room temperature. Figure 4 shows the experimental and fitting results for $\text{TbFe}_{1-x}\text{Mn}_x\text{O}_3$. Corresponding Eq. (1) with $x=0 \sim 0.6$ and parameters $x_c \approx 0.0080$ and $k' = 0.0060$ is adopted for this system. Since the Eq. (1) is only valid at low doping concentration, we can obtain good fitting up to $x=0.5$. As shown in Fig. 4, T_{SR}^1 could be taken as the onset point of the first spin reorientation transition, and T_{SR}^1 can be enhanced to 299 K at $x=0.5$. For $x > 0.6$, the spin reorientation transition phenomenon was not observed up to their Néel temperatures (T_N). Moreover, the T_N in Mn-rich $\text{TbFe}_{1-x}\text{Mn}_x\text{O}_3$ becomes much lower than that of the TbFeO_3 ($T_N=650$ K), since Mn doping could weaken both the Tb^{3+} - Fe^{3+} interaction and the Fe^{3+} - Fe^{3+} interaction. In the high temperature Γ_4 region of $\text{TbFe}_{1-x}\text{Mn}_x\text{O}_3$, the Tb^{3+} - Fe^{3+} interaction is much stronger than that of Fe^{3+} - Fe^{3+} interaction and the former one causes the parallel aligns between the moments of Tb^{3+} and Fe^{3+} to give rise to the net moments along c axis⁵. This scenario is supported from the magnetization behavior along c axis as indicated

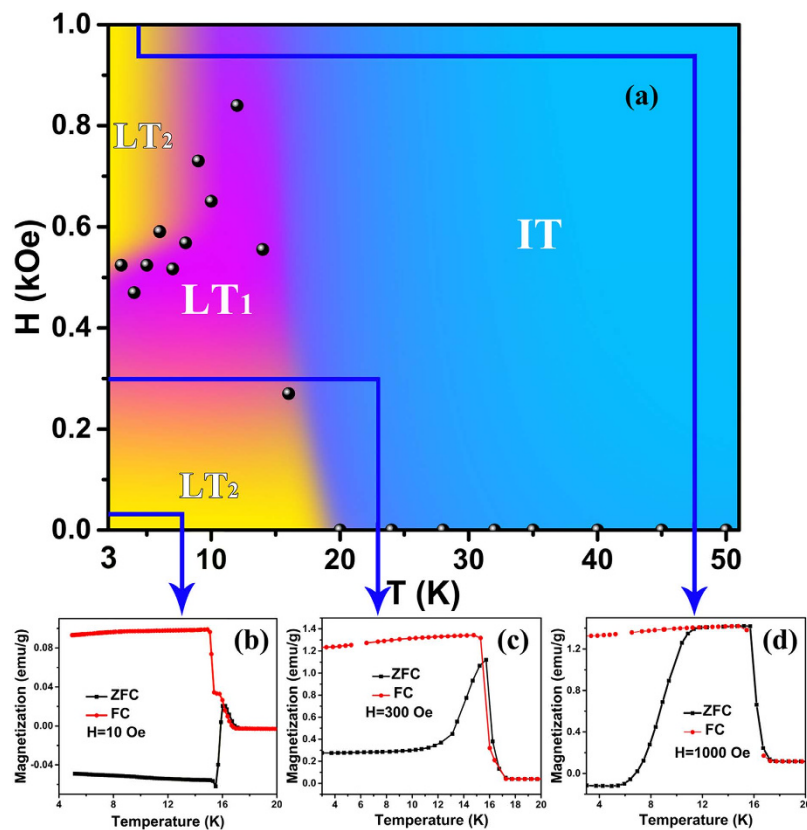


Figure 5. The phase diagram of magnetization vectors of $\text{TbFe}_{1-x}\text{Mn}_x\text{O}_3$ ($x=0.25$) by tuning the applied magnetic field and temperature. LT_1 : low temperature phase-1, LT_2 : low temperature phase-2, IT : intermediate temperature phase.

in Fig. 1(b). As a consequence, the substitution of Mn for Fe breaks the original Tb^{3+} - Fe^{3+} interaction, leading to the shift of T_{SR}^1 towards higher temperature³⁴.

Spin reorientation at T_{SR}^2 . Compare with the $\Gamma_4 \rightarrow \Gamma_1$ spin reorientation at T_{SR}^1 , the $\Gamma_1 \rightarrow \Gamma_4$ spin reorientation at T_{SR}^2 presents more complex magnetic phase since the ordering degree and interaction between magnetic ions get larger at low temperature. We herein take $\text{TbFe}_{0.75}\text{Mn}_{0.25}\text{O}_3$ as a representative of $\text{TbFe}_{1-x}\text{Mn}_x\text{O}_3$ system to discuss the characteristic of re-entrant $\Gamma_1 \rightarrow \Gamma_4$ spin reorientation. Figure 5(a) shows a phase diagram of magnetic field *versus* temperature for $x=0.25$, and the data points of crossover field H_{cro} were obtained from the isothermal M - H curves, in which H_{cro} is taken as the cross point between M^a - H and M^c - H curves (i.e. when $M^a = M^c$ at a given temperature) from $H=0$ kOe to 70 kOe. As the applied field increases, the M - T curves of the same system show dramatically different characteristics. The solid data points at the phase boundaries represent the second spin reorientation transition temperature T_{SR}^2 for $x=0.25$ sample, which divides the diagram into three magnetic phases, i.e., the first low temperature phase (LT_1), the second low temperature phase (LT_2), and intermediate temperature phase (IT). Both LT_1 and LT_2 phases are characterized as Γ_4 type, and IT is of Γ_1 type. LT_1 presents a weak ferromagnetic phase with Γ_4 type while LT_2 regions show the negative magnetization behavior with Γ_4 type. This phase diagram illustrates the phase transition $\Gamma_1 \rightarrow \Gamma_4$ can be modified by the external field at low temperature, resulting in rich variation of magnetocrystalline anisotropy.

Discussion

Several factors may affect the spin reorientation transition phenomena: single ion anisotropy, DM interaction, exchange interaction, and magnetic anisotropy³⁵. For a rare-earth ion, $4f$ orbital electrons make it special in bonding and the compounds have large single ion anisotropy. Consequently, the giant magnetocrystalline anisotropy and sharp spin reorientation can be attributed to the single ion anisotropy of Tb^{3+} with large angular momentum. For a spin-canted system^{36–39}, a ubiquitous antisymmetric interaction $\mathbf{D} \cdot (\mathbf{S}_1 \times \mathbf{S}_2)$ exists, which is linear with respect to the spin-orbit coupling and exchange interaction. The magnitude of \mathbf{D} can be expressed roughly as $D \approx (\Delta g)/(g)J_{\text{super}}$, where g is the gyromagnetic ratio, Δg is its deviation from the value for a free electron, and J_{super} is the strength of superexchange interaction. According to the magnetocaloric and NPD data, we can regard the magnetic entropy change between the a and c axes as a measurement of magnetocrystalline anisotropy energy and analyze the superexchange interactions in our $\text{TbFe}_{1-x}\text{Mn}_x\text{O}_3$ system.

In order to illustrate the variation of magnetocrystalline anisotropy energy *versus* Mn doping concentration, we estimate that the magnetic entropy change ($-\Delta S_M$, where $-\Delta S_M = (-\Delta S_M^a) - (-\Delta S_M^c)$) between the a and

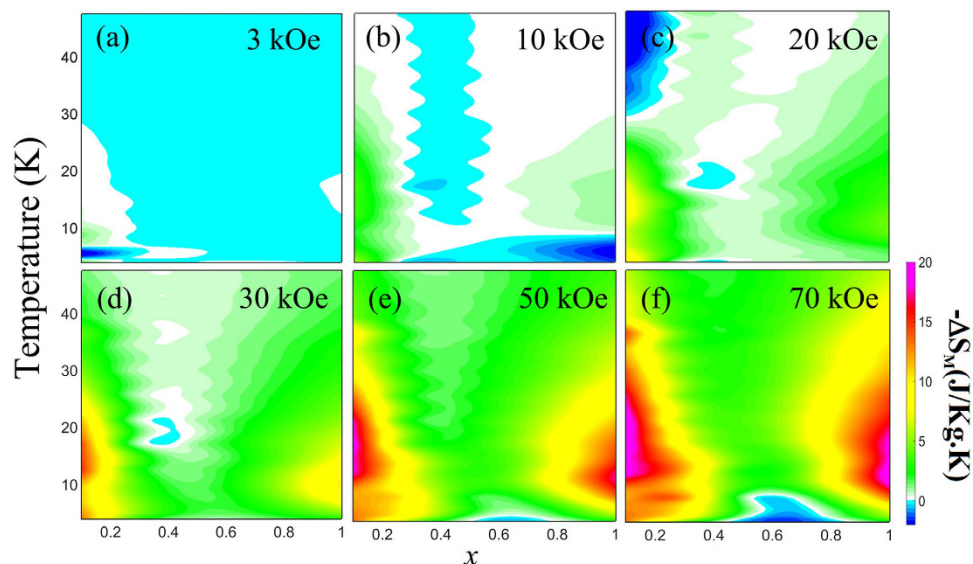


Figure 6. The distribution of magnetic entropy change as a function of the temperature and Mn concentration x under different applied fields. (a) $H = 3$ kOe, (b) $H = 10$ kOe, (c) $H = 20$ kOe, (d) $H = 30$ kOe, (e) $H = 50$ kOe, (f) $H = 70$ kOe.

c axes in $\text{TbFe}_{1-x}\text{Mn}_x\text{O}_3$ single crystals. According to Maxwell's relation^{40,41}, the magnetic entropy change in a thermodynamic process can be estimated using the following equation

$$\Delta S_M(T, \Delta H) = S_M(T, \Delta H) - S_M(T, 0) = \int_0^H \left(\frac{\partial S}{\partial H} \right) dH = \int_0^H \left(\frac{\partial M}{\partial T} \right) dH. \quad (2)$$

We take the $\Delta T = 1$ K (or no more than 5 K at higher temperature) and $\Delta H = 1$ kOe and the computed results are illustrated in Fig. 6(a–f). From Eq. (2), the magnetic entropy change is a function of both temperature and magnetic field. Therefore, by changing temperature and magnetic field, the direction of magnetization vector will rotate due to the magnetocrystalline anisotropy field, and the distribution of anisotropy energy will also vary. Hereafter, we denote the magnetocrystalline anisotropy energy as E_{ani} . It is noted that the $-\Delta S_M$ value decreases from $x = 0$ to $x = 0.5$ and then increases to $x = 1$, suggesting a similar tendency for the E_{ani} . The evolution of $-\Delta S_M$ versus doping concentration x implies that the superexchange interaction weakens along the c axis while enhances along the a or b axes for $0 \leq x \leq 0.5$, and the reversed case holds for $0.5 \leq x \leq 1$.

In $\text{TbFe}_{0.75}\text{Mn}_{0.25}\text{O}_3$, the hard axis is along the c direction, and the easy magnetization vector is along a direction as shown in Fig. 6. This contour plot of $-\Delta S_M$ reveals the state of E_{ani} , which may affect both the magnitude and the direction of magnetization vectors. Furthermore, it is noted that the magnitude of net magnetic moment is usually small but its direction is often a decisive factor when considering the exchange coupling interactions in a system⁴². According to our NPD experiment, the Tb^{3+} ions are in paramagnetic state at $T \geq 8$ K. Therefore, the Tb–Fe(Mn) interactions should be very weak so that they can hardly be influenced by the crystal field. As the applied field increases, ZFC magnetizations in Γ_4 phase become increasing larger, as shown by the ZFC–FC convergence near the Γ_4 – Γ_1 transition (Fig. 5b–d). Thus, the effect of the external field plays a determining role on Γ_4 – Γ_1 transition which to be explored in future.

According to the NPD experimental results^{15,29}, the evolution of spin configurations versus doping content x is schematically illustrated in the upper panels of Fig. 7(a–c). In the lower panels of Fig. 7(e,f), the spin glass (SG) transition T_{SG} occurs at 16 and 6.5 K along the c axis under $H = 100$ Oe in both $\text{TbFe}_{0.75}\text{Mn}_{0.25}\text{O}_3$ and TbMnO_3 single crystals, respectively. However, the SG state is not detected along any axis down to 1.9 K in TbFeO_3 single crystal from Fig. 7(d), nor a and b axes in $\text{TbFe}_{0.75}\text{Mn}_{0.25}\text{O}_3$ and TbMnO_3 single crystals. The observation of SG behavior is attributed to the competition between AFM and FM component, leading to a spin frustration in Fig. 7(e,f). The M–O–M bond angle ($M = \text{Fe}$ or Mn), namely, superexchange interaction angle, is usually reduced from 180° due to the cooperative octahedral rotations in the orthorhombic perovskites. In RMO_3 systems⁴³, the easy magnetization axis may rotate below T_N because of the coupling between magnetic moments of rare earth R ions and the spin of transition metal M ions. As the major controlling factor of the superexchange interaction, the coupling of M–O–M is much stronger than that of R–O–M, which should be neglected. In $\text{TbFe}_{1-x}\text{Mn}_x\text{O}_3$ system, the Fe–O–Fe interaction can be partially replaced by Fe–O–Mn upon Mn^{3+} doping. In Fig. 7(b,c), the spin frustration along c axis causes the anisotropic superexchange interaction decreasing along the c axis by Mn substitution, which means the entropy change between the a and c axis gets weaker as x increases in a Fe-rich $\text{TbFe}_{1-x}\text{Mn}_x\text{O}_3$ system. The mechanism of SG phenomena is as follows.

Since the ionic radius of Fe^{3+} is equal to Mn^{3+} in high spin state (Fe^{3+} : $S = 5/2$, $5.9 \mu_B/\text{at.}$, $r = 0.645 \text{ \AA}$ and Mn^{3+} : $S = 2$, $4.9 \mu_B/\text{at.}$, $r = 0.645 \text{ \AA}$), the crystal distortion caused by ionic radius difference can be ignored. It should be pointed out that the hybridization between inter-site t and e orbitals is orthogonal for a 180° M–O–M chemical bonding. The sketches of Fig. 8(a–c) describe the different effects of Mn^{3+} and Fe^{3+} ions on the orbital

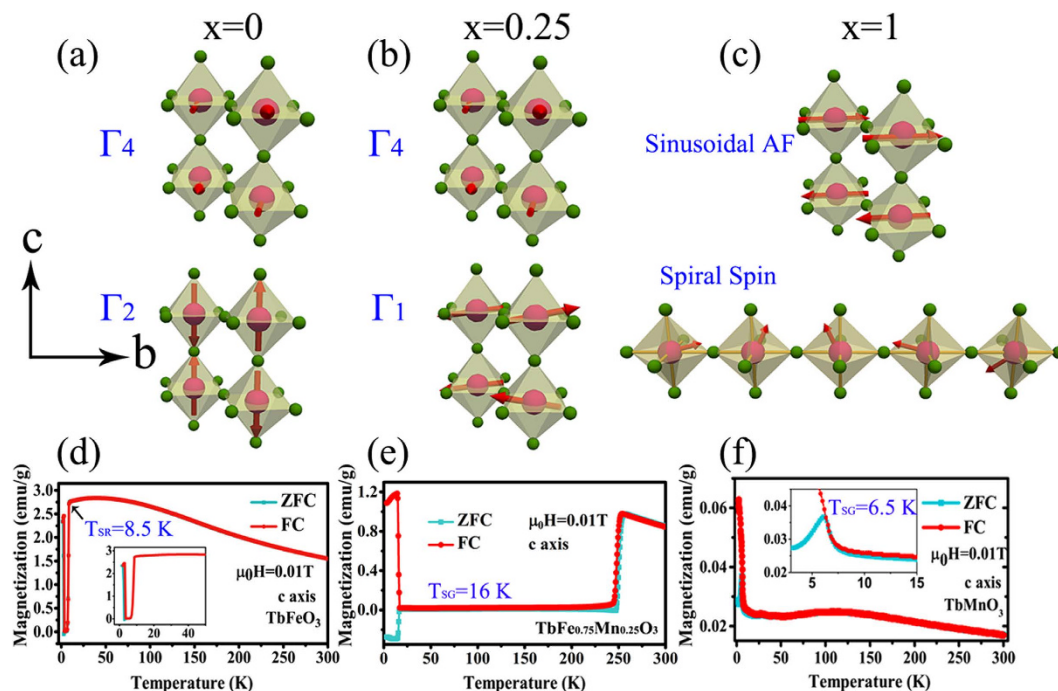


Figure 7. The spin configurations and spin glass state in $\text{TbFe}_{1-x}\text{Mn}_x\text{O}_3$ system. (a) $x=0$, no SG behavior down to 1.9 K, (b) $x=0.25$, SG transition at 16 K, (c) $x=1.0$, SG transition at 6.5 K. The sketches in upper panels show the variation of spin configurations in the bc -plane versus x and the lower panels show the M - T curves along the c axis under $H=100$ Oe.

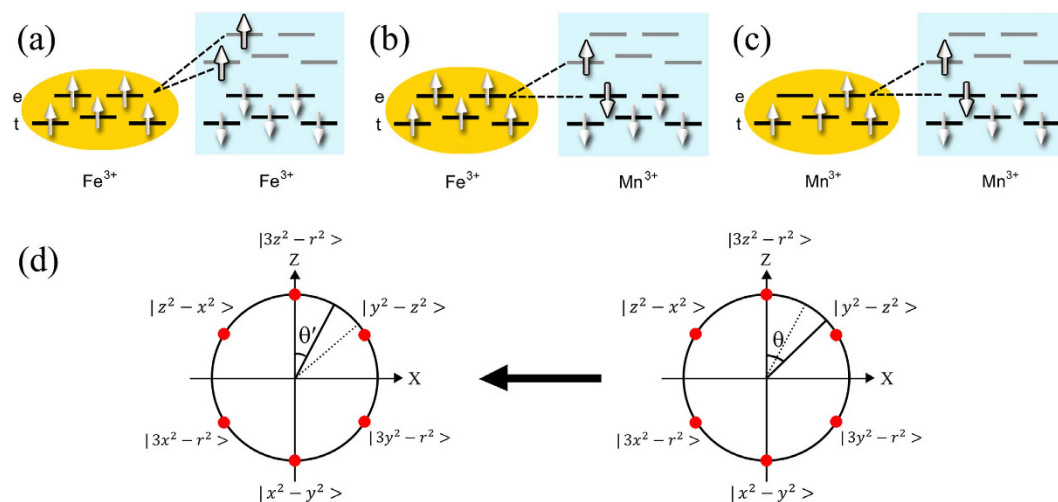


Figure 8. Schematic diagrams of the hybridization effect on the virtual charge transfer for (a) Fe-Fe, (b) Fe-Mn, (c) Mn-Mn, based on Goodenough-Kanamori rules in $\text{TbFe}_{1-x}\text{Mn}_x\text{O}_3$ system. The occupied state for electrons implicates that Mn substitution promotes the FM component. (d) The θ becomes smaller when Fe doping content increases, in accompany with the weaker lattice distortion.

hybridization. According to Goodenough-Kanamori rule⁴⁴, the superexchange interaction between two adjacent transition-metal ions is delivered by a virtual charge transfer. The Fe^{3+} and Mn^{3+} ions present different configurations for the outer shell electrons, i.e., t^2e^2 for Fe^{3+} and t^3e^1 for Mn^{3+} , respectively. In RFeO_3 , five outer shell electrons of Fe^{3+} ions lead to half-filled e_g (σ -bond component) and t_{2g} (π -bond component) orbitals. Therefore, the superexchange interactions between the two Fe^{3+} ions only result in an AFM coupling, in accordance to Hund's rules. For Mn^{3+} ions, there are three kinds of coupling, i.e., $t^3\text{-O-}t^3$, $e^1\text{-O-}e^1$ and $t^3\text{-O-}e^1$. The superexchange interactions over the half-filled $t^3\text{-O-}t^3$ induce an AFM coupling. Nevertheless, the hybridization between $t^3\text{-O-}e^1$ and $e^1\text{-O-}e^1$ might provide an FM coupling in the system, which experimentally confirms that the spiral spin states in TbMnO_3 originate from spin frustration²⁹. The above argument can help us explain the SG phenomena in Fig. 7(b,c).

Now we look at the Mn-rich $\text{TbFe}_{1-x}\text{Mn}_x\text{O}_3$ system. As illustrated in Fig. 8(b,c), the Mn substitution gives rise to the FM component in $\text{TbFe}_{1-x}\text{Mn}_x\text{O}_3$ system with two consequences. One is the appearance of spin-glass state in Fig. 7(b,c), and the other one is the variation of anisotropic $-\Delta S_M$. In $\text{TbFe}_{1-x}\text{Mn}_x\text{O}_3$ ($x > 0.5$), Mn^{3+} substitution can induce more FM component and lead to a stronger lattice distortion in the system. These factors induce a spin frustration state and result in the reduction of superexchange interaction. In RMnO_3 system, the occupied e_g orbital wavefunction of Mn is given by Eq. (3)

$$|\varphi\rangle = \cos\frac{\theta}{2}|3z^2 - r^2\rangle \pm \sin\frac{\theta}{2}|x^2 - y^2\rangle \quad (3)$$

where θ is the respective orbital component (Fig. 8(d)). The ground state of the system is given by any normalized linear combination of the two e_g orbitals in Eq. (3). In TbMnO_3 , the Jahn-Teller distortion of MnO_6 octahedral is a mode of elongating along one axis but shrinking in the other two axes. Since the rare-earth ferrites belong to Jahn-Teller inactive system, θ becomes smaller with doping from $x = 1$ to 0.5, and the shape of wavefunction $|\varphi\rangle$ will be stretched. Therefore, the distance of Mn(Fe)-Mn(Fe) along the c axis between the Mn(Fe) O_6 octahedra should be longer than that in TbMnO_3 . Thus the superexchange interaction in $\text{TbFe}_{1-x}\text{Mn}_x\text{O}_3$ is suppressed along the c axis. Additionally, the application of external magnetic field can increase the lattice distortion and enhance the DM interaction^{45,46}. The above discussions can account for the variation of $-\Delta S_M$ for $0.5 \leq x \leq 1$.

In summary, we observed a re-entrant spin reorientation of type $\Gamma_4 \rightarrow \Gamma_1 \rightarrow \Gamma_4$ in $\text{TbFe}_{0.75}\text{Mn}_{0.25}\text{O}_3$ perovskite system. Through neutron powder diffraction and magnetization measurements, we have observed the recurrent magnetic phase transitions at 254 and 16 K. With Mn doping, the spin configurations can be modified and the spin glass state emerges due to the competition between AFM and FM components. Furthermore, the first spin reorientation temperature increases from 8.5 K for $x = 0$ to 299 K for $x = 0.5$ $\text{TbFe}_{1-x}\text{Mn}_x\text{O}_3$ sample, which might be useful for developing spin-switching devices. We have found a rich phase diagram of magnetization by tuning the applied magnetic field and temperature. In the framework of Goodenough-Kanamori rule, we analyze the evolution of $-\Delta S_M$ versus Mn doping to reveal the unusual spin reorientation and abundant magnetic phase diagram. It is found that the $-\Delta S_M$ decreases for $0 \leq x \leq 0.5$ and increases for $0.5 \leq x \leq 1$. The evolution of $-\Delta S_M$ is attributed to the change of anisotropic interactions tuned by Mn doping concentration. Furthermore, in an ongoing project we have discovered similar results in Mn doped HoFeO_3 and DyFeO_3 , with Mn dopants in RFeO_3 triggering a rare phase transition from normal $\Gamma_4 \rightarrow \Gamma_2$ to re-entrant $\Gamma_4 \rightarrow \Gamma_1 \rightarrow \Gamma_4$ spin reorientation.

Methods

A series of Mn doped terbium orthoferrites $\text{TbFe}_{1-x}\text{Mn}_x\text{O}_3$ ($x = 0, 0.10, 0.25, 0.40, 0.50, 0.60, 0.70, 0.80, 0.90, 1$) polycrystalline samples were first synthesized by traditional solid state reaction method. Single crystals of $x = 0, 0.10, 0.25$ and 1 were then grown by using a four-mirror optical floating-zone furnace (FZ-T-10000-H-VI-P-SH, Crystal System Corp.). The phase purity, crystal quality, and crystallographic orientation were checked by powder X-ray diffraction (XRD) and back-reflection Laue XRD experiment, respectively. Magnetization measurements were performed on vibrating sample magnetometer (VSM) attached to a physical property measurement system (PPMS-9), and both zero-field-cooling (ZFC) and field-cooling (FC) modes were used. The NPD experiments at 8, 40, and 300 K were carried out on the thermal triple-axis spectrometer SV30 located at China Advanced Research Reactor (CARR) in China Institute of Atomic Energy, and the neutron powder diffractor at the Institute of Nuclear Physics and Chemistry, China Academic of Engineering Physics. The structural data analyses of XRD and NPD were performed by FullProf program using Rietveld method⁴⁷, and the magnetic symmetry analysis was performed with BasIReps.

References

1. Yamaguchi, K. *et al.* Terahertz Time-Domain Observation of Spin Reorientation in Orthoferrite ErFeO_3 through Magnetic Free Induction Decay. *Phys. Rev. Lett.* **110**, 137204 (2013).
2. Mikhailovskiy, R. V. *et al.* Terahertz emission spectroscopy of laser-induced spin dynamics in TmFeO_3 and ErFeO_3 orthoferrites. *Phys. Rev. B* **90**, 184405 (2014).
3. Tokunaga, Y. *et al.* Magnetic-Field-Induced Ferroelectric State in DyFeO_3 . *Phys. Rev. Lett.* **101**, 097205 (2008).
4. Kuo, C. Y. *et al.* $k = 0$ Magnetic Structure and Absence of Ferroelectricity in SmFeO_3 . *Phys. Rev. Lett.* **113**, 217203 (2014).
5. Artyukhin, S. *et al.* Solitonic lattice and Yukawa forces in the rare-earth orthoferrite TbFeO_3 . *Nat. Mater.* **11**, 694–699 (2012).
6. Tokura, Y. & Nagaosa, N. Orbital Physics in Transition-Metal Oxides. *Science* **288**, 462 (2000).
7. Jin, S. *et al.* Thousandfold Change in Resistivity in Magnetoresistive La-Ca-Mn-O Films. *Science* **264**, 413–415 (1994).
8. Salamon, M. B. & Jaime, M. The physics of manganites: Structure and transport. *Rev. Mod. Phys.* **73**, 583–628 (2001).
9. Solovyev, I., Hamada, N. & Terakura, K. Crucial Role of the Lattice Distortion in the Magnetism of LaMnO_3 . *Phys. Rev. Lett.* **76**, 4825–4828 (1996).
10. Dzyaloshinskii, I. Magnetolectric to multiferroic phase transitions. *Europhys. Lett.* **96**, 17001 (2011).
11. Astrov, D. N. The magnetolectric effect in antiferromagnets. *Sov. Phys. JETP* **11**, 708 (1960).
12. Kajimoto, R. *et al.* Magnetic structure of TbMnO_3 by neutron diffraction. *Phys. Rev. B* **70**, 012401 (2004).
13. Yoda, T., Yokoyama, T. & Murakami, S. Current-induced Orbital and Spin Magnetizations in Crystals with Helical Structure. *Sci. Rep.* **5**, 12024, doi: 10.1038/srep12024 (2015).
14. Kimura, T. *et al.* Magnetic control of ferroelectric polarization. *Nature (London)* **426**, 55–58 (2003).
15. Goto, T. *et al.* Ferroelectricity and Giant Magnetocapacitance in Perovskite Rare-Earth Manganites. *Phys. Rev. Lett.* **92**, 257201 (2004).
16. Koehler, W. C. *et al.* Neutron Diffraction Study of Magnetic Ordering in Thulium. In *Proceedings of the Seventh Conference on Magnetism and Magnetic Materials* (ed. Osborn, J. A.) 1124–1125 (Springer, 1962).
17. Chai, Y. S. *et al.* Electrical control of large magnetization reversal in a helimagnet. *Nat. Commun.* **5**, 4208, doi: 10.1038/ncomms5208 (2014).
18. Maleyev, S. V. Spin chirality and polarized neutrons. *Physica B* **350**, 26–32 (2004).
19. Okorokov, A. I. *et al.* The spin chirality in MnSi single crystal probed by small angle scattering with polarized neutrons. *Physica B* **350**, E323–E326 (2004).

20. Bertaut, E. F. *et al.* Structures magnetiques de TbFeO₃, *Solid State Commun.* **5**, 293–298 (1967).
21. Bertaut, E. F. In *Magnetism III* (ed. Rado, J. T. & Suhl, H.) 149–209 (Academic, 1963).
22. Bouree, J. E. & Hammann, J. Mise en évidence expérimentale des effets de forme dans l'orthoferrite de terbium. *J. Phys. (Paris)* **36**, 391 (1975).
23. Holmes, L., Van Uiter, L. G. & Hecker, R. Effect of Co on magnetic properties of ErFeO₃, HoFeO₃, and DyFeO₃. *J. Appl. Phys.* **42**, 657 (1971).
24. Gorodetsky, G., Sharon, B. & Shtrikman, S. Magnetic Properties of an Antiferromagnetic Orthoferrite. *J. Appl. Phys.* **39**, 1371 (1968).
25. Bozorth, R. M., Kramer, V. & Remeika, J. P. Exchange Fields and Optical Zeeman Effect in ErFeO₃. *Phys. Rev.* **185**, 689 (1969).
26. Helton, J. S. *et al.* Magnetic order of the hexagonal rare-earth manganite Dy_{0.5}Y_{0.5}MnO₃. *Phys. Rev. B* **84**, 064434 (2011).
27. Pierce, R. D., Wolfe, R. & VanUitert, L. G. Spin Reorientation in Mixed Samarium-Dysprosium Orthoferrites. *J. Appl. Phys.* **40**, 1241 (1969).
28. Wu, H. L. *et al.* Twofold spin reorientation and field-induced incomplete phase transition in single-crystal Dy_{0.5}Pr_{0.5}FeO₃. *Phys. Rev. B* **90**, 144415 (2014).
29. Tokura, Y. & Seki, S. Multiferroics with spiral spin orders. *Adv. Mater.* **22**, 1554 (2010).
30. Jin, J. L. *et al.* Giant anisotropy of magnetocaloric effect in TbMnO₃ single crystals. *Phys. Rev. B* **83**, 184431 (2011).
31. Kimura, T., Spiral Magnets as Magnetolectrics. *Ann. Rev. Mater. Res.* **37**, 387–413 (2007).
32. White, R. L. Review of Recent Work on the Magnetic and Spectroscopic Properties of the Rare-Earth Orthoferrites. *J. Appl. Phys.* **40**, 1061 (1969).
33. See supplemental information for details of the magnetic moments along different crystallographic axes for TbFe_{1-x}Mn_xO₃ (x = 0.25) single crystal.
34. Zhao, W. Y. *et al.* Spin reorientation transition in dysprosium-samarium orthoferrite single crystals. *Phys. Rev. B* **91**, 104425 (2015).
35. Hong, F. *et al.* Continuously tunable magnetic phase transitions in the DyMn_{1-x}Fe_xO₃ system. *Appl. Phys. Lett.* **99**, 092502 (2011).
36. Dmitrienko, V. E. *et al.* Measuring the Dzyaloshinskii-Moriya interaction in a weak ferromagnet. *Nat. Phys.* **10**, 202 (2014).
37. Moriya, T. New Mechanism of Anisotropic Superexchange Interaction. *Phys. Rev. Lett.* **4**, 228 (1960).
38. Moriya, T. Anisotropic Superexchange Interaction and Weak Ferromagnetism. *Phys. Rev.* **120**, 91 (1960).
39. Dzyaloshinsky, I. A thermodynamic theory of “weak” ferromagnetism of antiferromagnetics. *J. Phys. Chem. Solids* **4**, 241 (1958).
40. Gschneidner, K. A. Jr., Pecharsky, V. K. & Tsokol, A. O. Recent developments in magnetocaloric materials. *Rep. Prog. Phys.* **68**, 1479 (2005).
41. Huang, R. X. *et al.* Large rotating field entropy change in ErFeO₃ single crystal with angular distribution contribution. *Appl. Phys. Lett.* **103**, 162412 (2013).
42. Hu, C. D. Antiferromagnetism: Giving directions. *Nat. Phys.* **10**, 180 (2014).
43. Zhou, J. S. *et al.* Intrinsic structural distortion and superexchange interaction in the orthorhombic rare-earth perovskites RCrO₃. *Phys. Rev. B* **81**, 214115 (2010).
44. Goodenough, J. B. *Magnetism and the Chemical Bond* (Interscience, 1963).
45. Jung, J. S. *et al.* Lattice distortion accompanied by magnetization reversal in A-type antiferromagnetic manganites. *Phys. Rev. B* **85**, 174414 (2012).
46. Sagayama, H. *et al.* Magnetic-field effects on Jahn-Teller distortion in ferroelastic magnetic insulator Fe_{1-x}Mn_xCr₂O₄. *Appl. Phys. Lett.* **99**, 082506 (2011).
47. Rodriguez-Carvajal, J. Recent advances in magnetic structure determination by neutron powder diffraction. *Physica B* **192**, 55 (1993).

Acknowledgements

This work was supported by the National Natural Science Foundation of China (NSFC, Grants No. 11574194, 51372149), the National Key Basic Research Program of China (Grant No. 2015CB921600), the Eastern Scholar Program and the Shuguang Program (Grant No. 12SG34) from the Shanghai Municipal Education Commission, Shanghai Institute of Materials Genome from the Shanghai Municipal Science and Technology Commission.

Author Contributions

Y.F. and J.Z. conceived the project. Single crystal samples, characterizations and magnetometry measurements were grown and performed by Y.F., NPD data were taken by X.L., Y.F., L.H., X.C., L.X., G.S., Y.L., D.C. and C.-W.W., Y.F., Y.Y., X.L., J.K., V.C., Y.C. and S.C. have contributed to analyze the results, and Y.F., W.R., C.L., V.C., F.C. and J.Z. wrote the manuscript. All authors reviewed the manuscript.

Additional Information

Supplementary information accompanies this paper at <http://www.nature.com/srep>

Competing financial interests: The authors declare no competing financial interests.

How to cite this article: Fang, Y. *et al.* Observation of re-entrant spin reorientation in TbFe_{1-x}Mn_xO₃. *Sci. Rep.* **6**, 33448; doi: 10.1038/srep33448 (2016).



This work is licensed under a Creative Commons Attribution 4.0 International License. The images or other third party material in this article are included in the article's Creative Commons license, unless indicated otherwise in the credit line; if the material is not included under the Creative Commons license, users will need to obtain permission from the license holder to reproduce the material. To view a copy of this license, visit <http://creativecommons.org/licenses/by/4.0/>

© The Author(s) 2016